

## Research Article

# Imaging Algorithm for Sea-Surface Ship Targets Based on Block Sparsity

Zhang Lin  and Jiang Yicheng 

*School of Electronics and Information Engineering, Harbin Institute of Technology, Harbin 150001, China*

Correspondence should be addressed to Jiang Yicheng; [jiangyc@hit.edu.cn](mailto:jiangyc@hit.edu.cn)

Received 7 April 2020; Revised 30 June 2020; Accepted 16 July 2020; Published 22 September 2020

Academic Editor: Rodolfo Araneo

Copyright © 2020 Zhang Lin and Jiang Yicheng. This is an open access article distributed under the Creative Commons Attribution License, which permits unrestricted use, distribution, and reproduction in any medium, provided the original work is properly cited.

In this study, a phased array radar was used to accurately image stationary and moving ship targets on the vast sea surface. To solve the challenge in real-time processing of the massive amount of data generated by phased array synthetic-aperture radar imaging, this study leveraged the block sparse characteristics of ships on the sea surface and adopted the joint block orthogonal matching pursuit algorithm to obtain high-resolution one-dimensional range images. By only estimating the azimuth Doppler parameters of the targets within the range gates, the amount of process data was significantly reduced, and the data processing speed was enhanced. The synchrosqueezing transform-STFT algorithm was introduced to perform transient imaging as a solution to the blurred imaging of ships due to the three-dimensional swing under the action of waves. The images of the targets were obtained from different squint angles of the antenna array, which improved the imaging accuracy of ships on a vast sea surface. Compared with traditional imaging algorithms, this algorithm can effectively overcome the interference of sea clutter on ship imaging and the influence of sea waves on ship wobble; it can also obtain high-resolution imaging for both stationary and moving targets in a limited amount of time.

## 1. Introduction

The sea has a vast surface area, and the development of the quick and accurate imaging of ships on such a vast surface remains an objective for airborne or space-borne synthetic-aperture radar (SAR). Under the scenario of a vast sea surface, SAR images can be obtained using range-Doppler (RD) and other conventional synthetic-aperture imaging algorithms. In this study, a phased array airborne SAR was adopted. Compared with a single-channel SAR system, not only is the size of the antenna array increased and not only are the shortcomings of insufficient spatial data sampling solved, but also the mapping swath for the sea area is extended; thus, high-resolution images of the vast sea surface can be acquired. Therefore, the phased array airborne SAR plays an important role in military reconnaissance, ship management, marine dynamic monitoring, and other fields.

In recent years, many countries have been actively promoting the implementation and application of phased

array radar in the field of SAR imaging. Alenia Aeronautica, an Italian aerospace company, launched Plan “Compact-SAR” in 2015, which created an active phased array system capable of beam-pointing in azimuth and elevation planes [1]. The PAMIR active phased array, an airborne SAR/MTI (Moving Target Indication) experimental instrument developed in Germany, adopted the *Scan-GMTI* mode and space-time adaptive processing algorithm. It can rapidly detect moving targets at large scanning angles and wide areas and perform target detection and velocity estimation, as well as determining the positioning of moving ships [2]. In 2017, the UK designed and built the NovaSAR system, which was placed in the polar Sun-synchronous orbit. The system uses a multimode active phased array and beamforming components to achieve ship detection and sea imaging with the sea clutter background [3]. Phased array SAR was developed based on single-channel SAR. The imaging of ships on the sea surface is different from that of ground stationary targets. Due to the influence of sea waves, the hull will rotate and

generate high-order Doppler frequencies. To obtain high-resolution images of ship targets, the range-instantaneous Doppler (RID) imaging method is usually used to focus the targets, such that the positions of the targets' scattering points at each range unit are only related to their instantaneous Doppler frequency [4]. The RID algorithm can be classified into two categories: nonparametric and parametric. Among these, the former algorithm mainly obtains the targets' transient Doppler images using the time-frequency analysis method, while the latter models the echo as a multicomponent polynomial phase signal and estimates its parameters [5]. In a study using the time-frequency analysis method conducted by Ling Wang, a single target was first extracted from the SAR image domain; then, the half-window correlation alignment method was applied to align the envelope. Afterward, the phase gradient autofocus (PGA) algorithm was applied to compensate the azimuth phase; finally, the images of ship targets were obtained through time-frequency analysis [6]. In a study using a nonparametric method conducted by Xia Bai, a parameter estimation method was constructed by combining Chirp-Z transform and scaled Fourier transform, which estimated the multicomponent secondary frequency modulation signals after range compression and motion compensation of ship targets [4]. Based on the bilinear extended fractional Fourier transform, Zhen estimated the Doppler center and quadratic Doppler frequency of a nonuniformly rotating ship and compensated the multicomponent cubic phase signal after motion [7]. Wang first separated the ship targets and then used the *Radon-Wigner* transform to estimate the Doppler parameters and complete focusing the targets [8]. Meanwhile, Marco applied the cell-averaging-CFAR (CA-CFAR) moving targets detection method to automatically detect the ship targets from the entire scene; the local polynomial Fourier transform algorithm was used to estimate the Doppler parameters, and the inverse SAR (ISAR) ship targets were autofocused using the image contrast autofocus algorithm [9].

The methods used in the above studies achieved focused imaging of ship swing under sea conditions, but they all exhibited certain limitations. First, due to the vast sea surface area, the amount of imaging transmission data is relatively large, which is not conducive to the long time-of-flight imaging of the vast sea surface. Second, the parameterization method not only involves a more complicated algorithm but also requires stricter application conditions. This algorithm is mainly used for the calibration compensation of second- and third-order phase errors. Furthermore, the traditional time-frequency analysis method must compromise between the bilinear cross-term and the reduced resolution due to the inherent limitation of the uncertainty principle. To address these problems, this study applied the block sparse time-frequency analysis method for the phased array radar imaging of the vast sea surface based on the existing algorithms. First, the block sparsity-based joint block orthogonal matching pursuit (JBOMP) algorithm was adopted for joint one-dimensional (1D) range imaging. The strong correlation between the echoes of ship targets was used as the primary criterion for determining the block sparsity. In addition, the

range positions of the ship targets were obtained. This could help to locate and acquire data of the targets, greatly reducing the data processing volume for the array antenna. Then, the Keystone algorithm was adopted to perform the unified range migration correction of stationary and moving targets. The cross-correlation envelope alignment and Doppler parameter estimation were applied to complete azimuth phase compensation, and the PGA algorithm was used to complete azimuth coarse focusing. Finally, the synchrosqueezing transform-STFT algorithm was used to perform transient imaging of each target at the sampling time, achieving accurate imaging of ships on the vast sea surface. This algorithm could help overcome interference from sea clutter to the sparse blocks. Moreover, it ensures the consistency of the target's positions between arrays, which is conducive to the subsequent sparse reconstruction processing. Simultaneously, the areas where the targets were located could be further clarified, which reduces the calculation amount and time. Thus, this algorithm will play a positive role in the engineering application of phased arrays.

## 2. System Model

According to the Rayleigh roughness criterion, at a given incident angle, the surface roughness will be less than a certain value (related to the incident wavelength). Therefore, the slightly fluctuating sea surface can be regarded as "flat" for the radar incident waves, which are approximately specularly reflected. As a result, the radar cannot receive or can only receive a small number of echoes; thus, most of the relatively "flat" areas appear almost completely black in SAR images [10]. Ship targets on the sea surface occupy only a small number of units; therefore, they present very strong block sparsities in the range-Doppler plane. More specifically, whether the targets are moving or not, the block sparse characteristics are satisfied in both the range and azimuth dimensions of the vast sea surface. By leveraging this sparsity, the problems faced by phased array radar SAR imaging can be better solved. For example, one problem involves the storage and processing of the massive data generated by increasing the number of arrays or extending the antenna pulse intervals to obtain an imaging map with a larger scanning swath. Therefore, this paper proposes the establishment of joint block sparse SAR imaging model.

*2.1. Joint Block Sparse Synthetic-Aperture Radar Imaging Model.* As shown in Figure 1, a phased array aircraft was assumed to fly over a section of the sea surface in a straight line at a velocity  $V$ . To solve the problem of cofrequency interference, each array antenna used a linear frequency-modulated signal at a step frequency to collect echoes from the sea surface at multiple angles and multiple frequencies:  $f_m = f_0 + m\Delta f$  is the carrier frequency of the  $m$ -th array pulse;  $t_m$  is the slow time in the azimuth direction;  $K$  is the number of scattering points;  $M$  is the number of antennas;  $d$  ( $d = -M/2, \dots, M/2$ ) is the antenna array spacing;  $\theta$  is antenna pitch angle;  $V_y$  is the radial velocity; and  $V_a$  is the along velocity of the point target.  $R_{k,i}$  is the distance between

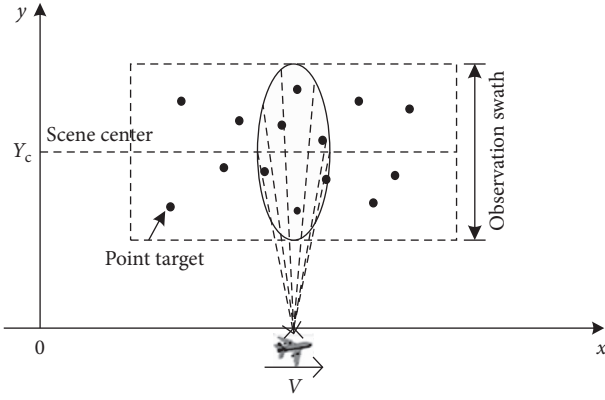


FIGURE 1: Geometric schematic diagram of SAR mode.

the  $k$ -th scattering point and the  $i$ -th channel, which can be expressed as

$$R_{k,i}(t_m) = R_0(i) - V_y(k) \cdot t_m + \frac{(V_a(k) - V)^2}{2R_0(i)} t_m^2, \quad (1)$$

$$R_0(i) = R_0 + i * d \sin \theta.$$

The echo signal of each pulse transmitted by the array can be recorded as a measurement vector, and the echo signal of  $K$  scattering points can be expressed as follows:

$$S_r = \sum_{k=1}^K \sigma_k \exp\left(j\pi\gamma(t - \tau_k)^2 \cdot \exp\left(\frac{-j4\pi f_m R_{k,i}(t_m)}{c}\right)\right), \quad (2)$$

where  $\sigma_k$  is the scattering coefficient of the  $k$ -th scattering point;  $\tau_k$  is the echo delay time of the  $k$ -th scattering point, which depends on the distance from the scattering point to the antenna array. As the ship targets satisfy the block sparse characteristics in the entire imaging area, their 1D range images are discretely distributed in limited areas within the range gates. By constructing an overcomplete basis  $\Theta$ , the data observed at the  $n_a$ -th azimuth position can be expressed as

$$s(n_a) = \Theta(n_a)x(n_a), \quad n_a = 1 \cdots N_a, \quad (3)$$

where  $N_a$  is the number of azimuth sampling points, and the range images of all arrays are sparse coded at each azimuth sampling time. As the change in array antenna spacing is negligible compared to the vertical distance of the range image  $R_{k,i}(t_m)$ , it can be considered that the sparse representations of echoes from the targets received by each antenna are consistent in the range direction. More specifically, the echo expression is based on the reflections from scattering points of the same target structure. By judging the consistency of sparse representations in the range dimension, the range gates targets located were obtained. By further screening the above sparse representations using CA-CFAR target detection, the sea clutter areas were eliminated [9]. Thus, the phased array beam could be focused on the limited range gates where the targets were located, and 1D range images with a higher resolution could

be obtained. This can also help to estimate the Doppler parameters of the moving ships.

This study adopted the compressed sensing algorithm to preserve the original structure of the sea surface targets with a small number of measurements. For the vast sea surface, the echo signals of the ship targets have common support sets in each channel of the range dimension. Thus, the targets can be considered to be at the same range gate, which is consistent with the multiple-measurement vector model. Under the condition that the channel amplitude-frequency characteristics are consistent, when the step frequency is irradiated to the same targets, for the same azimuth time, the sparse signal representations of adjacent echoes between arrays should have a strong correlation in the range direction. This correlation was used to build the joint block sparse model.

The nonzero scattering points of the 1D range images of the surface ships meet the block sparsity characteristics and are usually clustered within several range gates, as shown in Figure 2. The features of sparse block structures can be observed. When there are  $K$  scattering points in the scene, then at a certain sampling time, there are several sparse block structures in the range gate. After obtaining the positions of these sparse block structures, the beam-pointing can then be controlled to direct the beam uniformly toward the range gates where the targets are located, thereby improving the resolution and efficiency of imaging.

**2.2. Obtaining 1D Range Image Using Joint Block Orthogonal Matching Pursuit Algorithm.** The traditional block sparse algorithm uses the block orthogonal matching pursuit (BOMP), which is a compression-sensing reconstruction algorithm based on subspace block sparse signals. It marks all the information-supporting blocks of the signal through iteration and reconstructs the original signal by pseudo-inverse operation [11]. The BOMP algorithm has a relatively good universal application. However, for signals with a block sparsity of  $K$ , it takes at least  $K$  iterations to recover the source signal, and the algorithm efficiency is low [12]. Therefore, based on BOMP, this paper proposes a joint block orthogonal matching pursuit (JBOMP) algorithm by leveraging the phased array antenna structure. By correlating the independent judgment results of each antenna, this algorithm can screen out subblocks that contain nonzero scattering points more accurately and uniformly determine the position information of the targets, thereby further enhancing the suppression effect on the sea clutters. Thus, the positions of the targets can be quickly located on the vast sea surface without iterative processing.

Step 1: build a block sparse model of the ship targets on the 1D range image [13].

The echo signal  $x(n_a)$  in the range direction was divided into  $G$  subblocks, the number of which is related to the number of sea surface targets.  $x(n_a)$  can be expressed as  $x(n_a) = [x_1(n_a), \dots, x_g(n_a), \dots, x_G(n_a)]$ . At this point, the nonzero elements of the sea surface echo would appear in a few subblocks above.

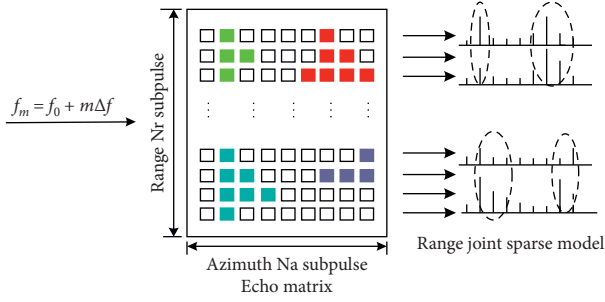


FIGURE 2: Joint block sparse schematic diagram in range dimension.

Depending on the target size, the length of each subblock was uneven and can be expressed as  $x_g(n_a) = x(g_1, n_a), \dots, x(g_j, n_a), \dots, x(g_q, n_a)$ . Each subblock  $x_g(n_a)$  contained  $q$  information components; that is, the subblock was the echo that selected  $x(g_1, \dots, g_q)$ . At this point, the range-dimensional sparse model of the  $N_a$  groups of echoes can be transformed into

$$\begin{cases} \hat{X} = \arg \min_{\hat{X}} \sum_{n_a=1}^{N_a} \sum_{g=1}^G I(\|x_g(n_a)\| > A), \\ \text{st } s(n_a) = \Theta_{n_a} x(n_a), \quad \forall n_a \in \{1, 2, \dots, N_a\}. \end{cases} \quad (4)$$

Formula (4) shows that  $x_g(n_a)$  only existed in a limited number of range units, and the amplitude was greater than the set threshold  $A$ . The minimum value of  $X$  indicates that the signal is the sparsest at this time, and it satisfies the observation equation. The subblock  $x_g(n_a)$  represents the targets' range images observed from the  $n_a$ -th azimuth position. By taking the union set of the sparse blocks of each antenna, multitargets range images with suppressed sea clutter could be obtained.

Step 2: select the observation matrix  $\Theta_g(n_a)$  and traverse the antenna echo signals to obtain the inner product sum of each subblock.

When the effect of sea clutter on the targets is limited, each column vector of the block sparse matrix  $X$  should have the same structural features; that is, the positions of nonzero elements in the vector are consistent. Therefore, the observed basis matrix  $\Theta_{n_a}$  was set as a function related to the azimuth, and the step frequency  $f_m$  corresponds to each receiving antenna. The expression for this is given by

$$\begin{aligned} \Theta(t_m) &= \text{rect}\left(\frac{t - 2R(t_m)/c}{T}\right) \cdot \exp\left(\frac{-j4\pi f_m R(t_m)}{c}\right), \\ m &= 1, \dots, M. \end{aligned} \quad (5)$$

Based on the best matching criteria between the received signals and the observation matrix  $\Theta_g(n_a)$ , formula 6 was used to calculate the inner product sum  $\hat{u}_g(l)$  of each subblock, where  $\langle \cdot \rangle$  indicates the inner product operations of echo signals at the array antenna frequency  $f_m$  with the observation matrix  $\Theta_g(n_a)$  at the corresponding frequency. If there were targets in the subblock in the range dimension, then the inner product sum will be larger than the sea clutter threshold.

$$\hat{u}_g(l) = \left( \sum_{g=1,2,\dots,G} \langle x_g(n_a), \Theta_g(n_a) \rangle \right) > A, \quad n_a = 1, 2, \dots, N_a. \quad (6)$$

Step 3: obtain the ranges of the subblock areas where the targets were located.

The corresponding position  $\lambda_g$  of the target subblock was determined using the following formula:

$$\lambda_g = \arg \max_{g=1,2,\dots,G} \left( \hat{u}_g(l) \right), \quad l = 1, 2, \dots, d. \quad (7)$$

After the coherence of different frequencies, if the selected range gates were adjacent or close, they were combined to form a sparse subblock. By traversing all the range units of the echo, areas with relatively few sparse blocks were finally determined as the target areas.

**2.3. Obtaining Ship Target Image Using the Synchrosqueezing Transform-STFT Algorithm.** As the movements of surface ships were unknown, there could be radial and along velocity or acceleration. Radial velocity would lead to a Doppler center shift; radial acceleration and along velocity would result in second- and high-order phases of the scattering point echo, causing defocused images of ships. Meanwhile, the ships exhibited 3D swing motion under the action of waves, resulting in nonstationary signals. The superposition of such signals would make it difficult to estimate the transient high-order phase error. Therefore, the time-frequency analysis of ISAR imaging was introduced to solve the image blur caused by the targets' wobble motion.

Synchrosqueezing transform (SST) is a new time-frequency reassignment postprocessing method proposed by Daubechies in 2011 [14]. Compared with the traditional time-frequency analysis algorithms, such as short-time Fourier transform (STFT) and continuous wavelet transform (CWT), the SST algorithm can break the Heisenberg uncertainty principle and provide a higher degree of time-frequency aggregation [15]. It also guarantees the strict mathematical sense of the inverse transformation, which helps to decompose the azimuth nonstationary and non-linear signals to obtain the transient time-frequency spectrum image. Let the azimuth echo signal with multiple component frequencies be

$$f(t) = \sum_{k=1}^K f_k(t), \quad (8)$$

$$f_k(t) = A_k(t) \exp \left\{ -j \frac{4\pi f_m}{c} [R(t) + R_r^k(t)] \right\},$$

where  $f_k(t)$  is the azimuth echo signal with  $k$  frequency components,  $A_k$  is the instantaneous amplitude of the echo,  $R(t)$  is the distance from the scattering point to the airborne radar array, and  $R_r^k(t)$  is the distance jitter resulting from the 3D rotation of the ship. For a finite  $k \in N$ , the STFT of signal  $f(t)$  can be expressed as

$$V_f^g(t, \eta) = \int_{-\infty}^{\infty} f(\tau) g(\tau - t) \cdot e^{-i2\pi\eta(\tau - t)} d\tau, \quad (9)$$

where  $\tau$  is the window length and  $g(\tau - t)$  is a compactly supported window function that can move with time  $t$ , which is used to intercept time-domain signals  $f(t)$ . By performing STFT transform on the intercepted signals, the local frequency spectrum information of signal  $f$  at time  $t$  can be obtained. By moving the window function along the entire time axis, the complete time-frequency distribution of signal  $f$  can be obtained. The SST-STFT algorithm based on STFT can be expressed as follows:

$$T_f^{g,\gamma}(t, \omega) = \frac{1}{g^*(0)} \int_{\left\{ \eta, |V_f^g(t, \eta)| > \gamma \right\}} V_f^g(t, \eta) \delta(\omega - \omega_f(t, \eta)) d\eta, \quad (10)$$

where  $\gamma$  is the threshold,  $\delta$  is the Dirac distribution, and  $\omega_f(t, \eta)$  represents the instantaneous frequency estimate at time  $t$  and frequency  $\eta$ , which can be expressed as

$$\omega_f(t, \eta) = R \left\{ \frac{\partial_t V_f^g(t, \eta)}{i2\pi V_f^g(t, \eta)} \right\}, \quad (11)$$

where  $R(Z)$  represents the real part of the complex number  $Z$  and  $\partial_t$  denotes the partial derivative of time  $t$ . It can be seen that, in the synchrosqueezing process, the time-frequency coefficients of the signal were distributed near the instantaneous frequency after STFT, which were concentrated at the instantaneous frequency  $\omega_f(t, \eta)$  through aggregation by function  $\delta$ . The SST cleverly leveraged the relationship between STFT and its partial derivative of time to estimate the instantaneous frequency of the signal at time  $t$ . Moreover, as the principle of SST-STFT involves the reassignment of the STFT complex spectrum along the frequency axis, this process is reversible, and the reconstructed original signal  $f(t)$  can be expressed as follows:

$$f(t) = \int_{\left\{ \omega, |w - \phi(k)| < d \right\}} T_f^{g,\gamma}(t, \omega) d\omega, \quad (12)$$

where  $\phi(k)$  is the estimated instantaneous frequency curve and  $d$  is the integration interval. The original azimuth signal can be obtained by integrating the SST-STFT transform coefficient at each time point. By utilizing the synchrosqueezing algorithm, highly aggregated time-frequency distribution curves can be extracted; the representation of

the time-frequency distribution energy can be enhanced; and the high-resolution imaging of multiple ships on the vast sea surface can be completed.

### 3. Simulation and Measured Data Imaging

*3.1. Theoretical Simulation.* This study used a simulation method that set three ships on the vast sea surface, one of which was stationary, and the other two were moving. The moving ships had both along and radial velocities. The parameter settings are detailed in Table 1. The algorithm flowchart is shown in Figure 3.

The 10-antenna airborne phased array radar was used for SAR imaging, and the JBOMP algorithm was applied to obtain the sparse block position of the target. Compared with the traditional sparse algorithms, OMP, BOMP, and Bayesian sparse algorithms, the JBOMP has better performance in running time, reconstruction error, and peak signal-to-noise ratio, as shown in Table 2.

Figure 4 shows the imaging results of the three ships using the JBOMP algorithm in the range direction. Here, it can be observed that the targets exhibited block sparse characteristics in the vast sea surface scene, and the positions of the subblocks can be clearly seen. Figure 5 shows that the original signal is sparsely measured by orthogonal matching pursuit OMP algorithm and joint block sparse JBOMP algorithm, respectively, and then the signal is reconstructed by the measured value. It can be seen that the JBOMP reconstruction signal can completely overlap with the original signal, and the reconstruction error is very small.

Because the stationary ship target displayed 3D swing motion (angular frequency of 0.1 rad/s) under the action of waves, conventional RD imaging would result in a defocused and blurry target, as shown in Figure 6(b). The Wigner-Ville distribution (WVD), STFT, adaptive linear chirplet decomposition, and the SST-STFT algorithm proposed in this paper were applied to perform the time-frequency analysis on ship 1. The time-frequency spectra are shown in Figures 6(c)–6(f). A comparison of the simulation results showed that the transient image obtained by the WVD algorithm had a blurred target, and the boundary of the ship was unclear. This was mainly due to the severe cross-terms generated by the algorithm when processing multicomponent signals. After STFT, the time-frequency coefficients were distributed near the instantaneous frequency, and the ship model could be seen in the resulting image. However, as limited by the length of the compactly supported window function, the time-frequency spectrum was blurred due to energy leakage, which reduced the imaging resolution. Through the parameter search estimation of the basis function, the adaptive chirplet decomposition algorithm decomposed the echo of each range unit and then integrated all the basis function signal components, which was time-consuming. Furthermore, the algorithm did not consider the correlations between the internal structures of the target; thus, it tended to fragment the target. The SST-STFT algorithm can accurately obtain the local frequency spectrum information of the target as well as the complete time-frequency distribution. The imaging took less time and did not

TABLE 1: Simulation parameters of surface ships.

Carrier frequency (GHz)	1.5
Scene center slant range (km)	3
Carrier speed (m/s)	300
Number of phased array antennas	10
Antenna spacing (m)	0.6
Pulse repetition frequency (Hz)	600
Transmit pulse width (us)	1.5
Transmit bandwidth (MHz)	150
A/D sampling rate (MHz)	300
Initial coordinates of ship 1 ( $X, Y$ )	(-80, -60)
Ship radial velocity ( $V_r$ ) (m/s)	0
Ship along velocity ( $V_a$ ) (m/s)	0
Initial coordinates of ship 2 ( $X, Y$ )	(0, 0)
Ship radial velocity ( $V_r$ ) (m/s)	40
Ship along velocity ( $V_a$ ) (m/s)	20
Initial coordinates of ship 3 ( $X, Y$ )	(100, 120)
Ship radial velocity ( $V_r$ ) (m/s)	-20
Ship along velocity ( $V_a$ ) (m/s)	-40

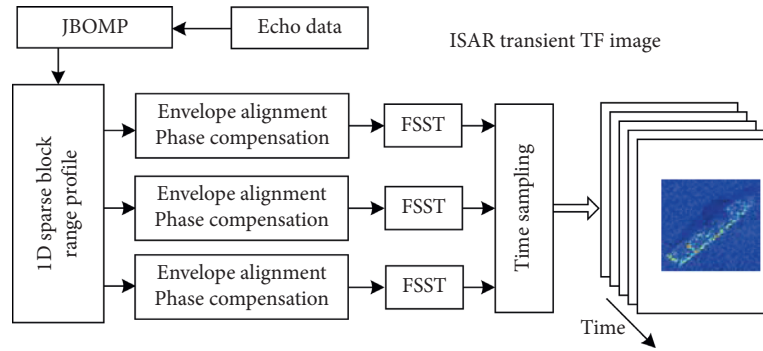


FIGURE 3: Flowchart of the block sparse-time-frequency analysis algorithm.

TABLE 2: Performance comparison of multiple algorithms.

	OMP	BOMP	BSBL	JBOMP
Running time (/s)	37.0561	9.4327	2.3627	7.5836
Reconstruction error (dB)	-12.1321	-12.2671	3.1849	-12.4313
PSNR (peak SNR)	60.2629	60.3979	44.9459	60.5879

show the phenomenon of energy diffusion. Therefore, this algorithm is more suitable for the phased array antenna imaging of ships on the sea surface.

Each antenna of the phased array can obtain a separate transient image. However, due to the spacing between the antennas, the squint angles of the antennas, as well as the received echo signals, differed. During the imaging process, transient images of the ship could be obtained from different angles. The resulting images from all angles could be integrated to generate a more comprehensive and accurate image. Figures 7(a)–7(h) are the resulting images acquired, respectively, by the equally spaced antennas, 1, 4, 7, and 10 of the antenna arrays and processed using the STFT and SST-STFT algorithms. A comparison of the simulation results showed that different antennas had different incidence angles for irradiating the ship target; the resulting images

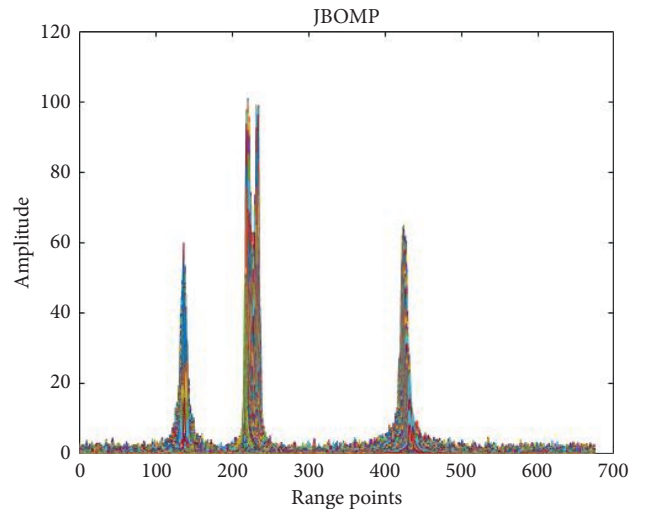


FIGURE 4: JBOMP signal in the range direction.

were similar, but there remained slight differences. From the target image obtained by the STFT algorithm, the key information regarding the ship (i.e., size, style, and levels) can be observed. In particular, the higher level of the hull can be distinguished from the bottom according to the varying

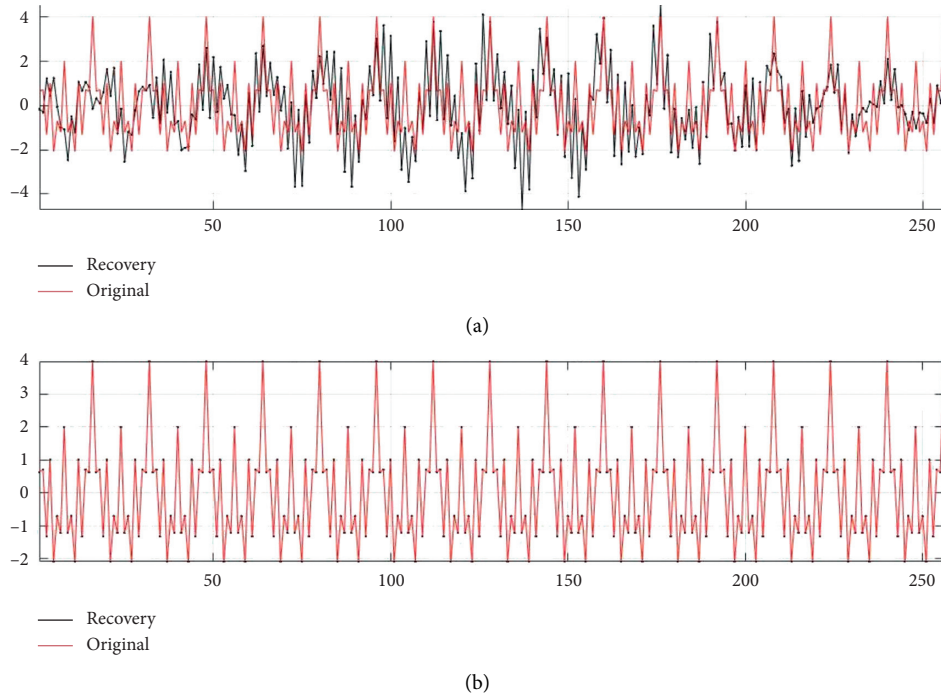


FIGURE 5: Reconstruction of OMP and JBOMP. (a) Comparison between OMP reconstructed signal and original signal. (b) Comparison between block sparse reconstruction signal and original signal.

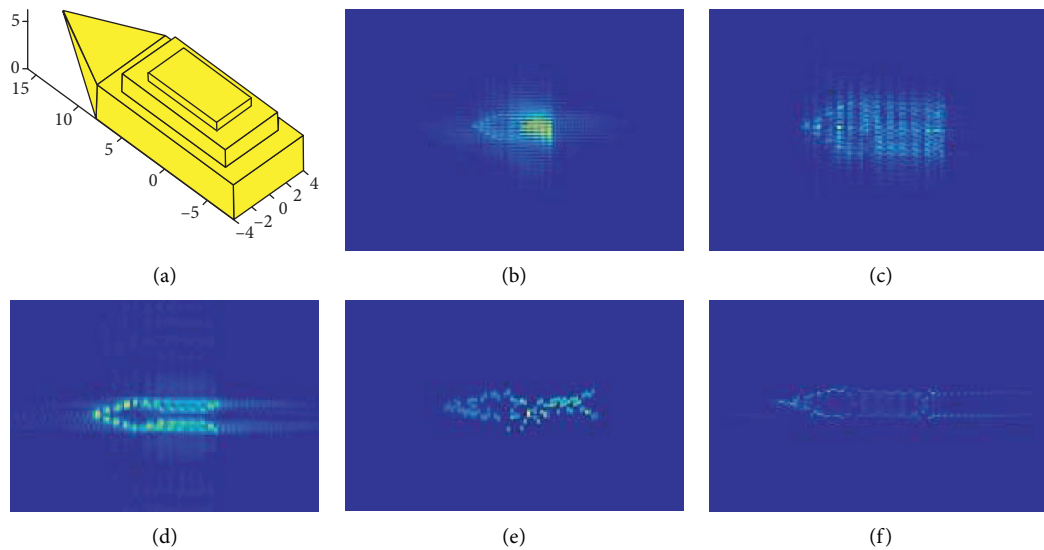


FIGURE 6: (a) Ship model; (b) RD ship imaging; (c) WVD ship imaging; (d) STFT ship imaging; (e) chirplet ship imaging; and (f) SST-STFT ship imaging.

colors on the time-frequency spectrum. The contour structure features of each level of the ship extracted using SST-STFT were finer. The Doppler frequency shift differences of scattering bodies on the top and bottom of the ship could be visually observed to determine its boundary and structure. Therefore, phased array radar has the advantage of angular diversity gain for the accurate imaging of ship targets.

**3.2. Measured Data.** The above simulation process verified the effectiveness of the algorithm. The measured data of a certain sea area in China were used to validate this ship imaging algorithm further. The RD imaging algorithm was applied to the measured data, and the Doppler parameters were estimated through the inertial navigation coefficient. Additionally, the dechirp algorithm was applied to complete

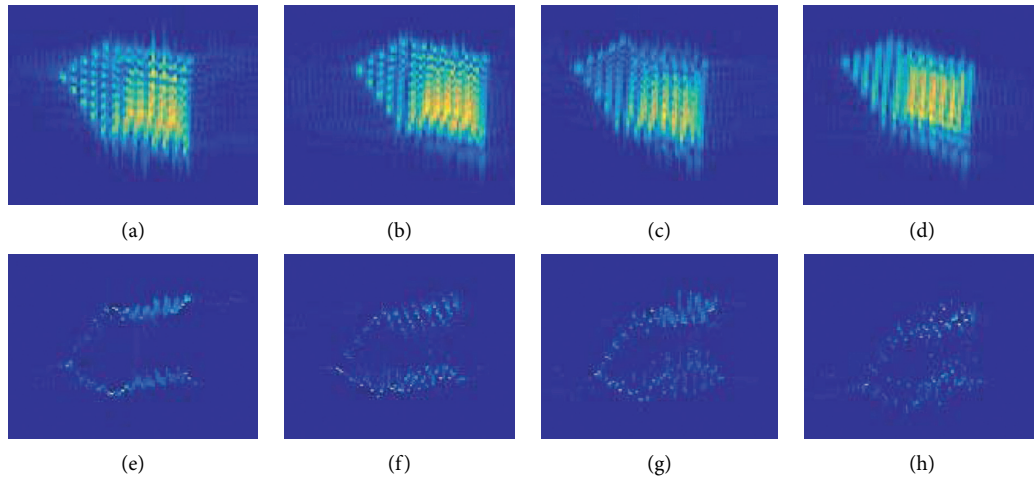


FIGURE 7: (a) Ant1 STFT; (b) Ant4 STFT; (c) Ant7 STFT; (d) Ant10 STFT; (e) Ant1 SST-STFT; (f) Ant4 SST-STFT; (g) Ant7 SST-STFT; and (h) Ant10 SST-STFT.

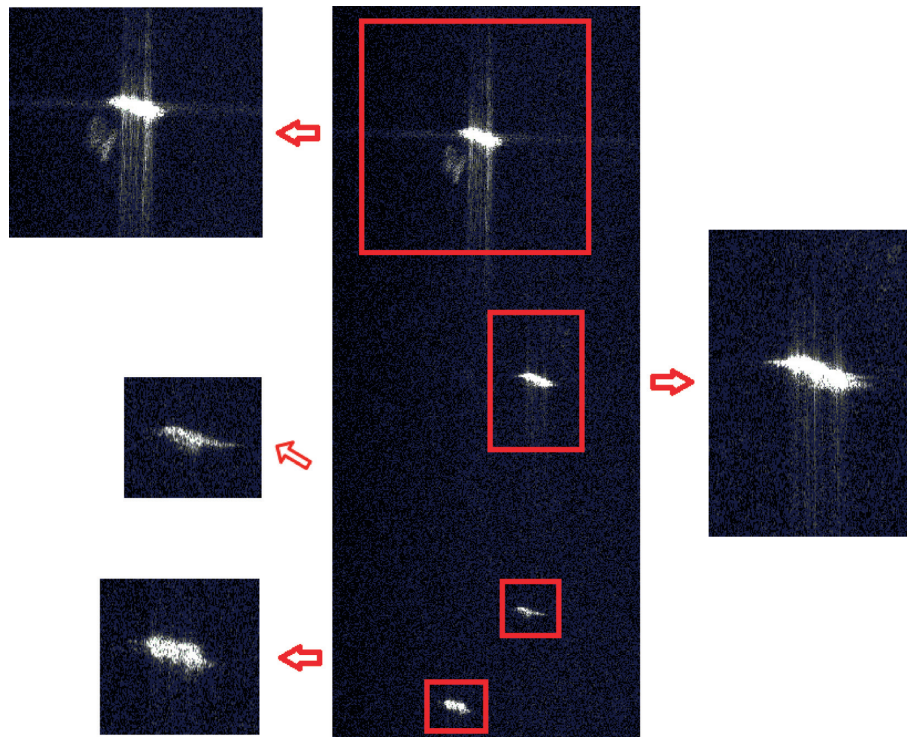


FIGURE 8: Scenario of measured data for the sea.

the azimuth focusing process. The imaging results are shown in Figure 8. The ship in the figure was affected by the 3D swing motion, and the echoes from the target's micromoving parts overlapped with its main body echo signal, which resulted in severe interference and caused the defocused and blurred view in the range direction. This observation was mainly caused by the rolling motion of the ship.

In Figure 9(a), a ghost shadow can be observed near the ship. This originates from the high-frequency vibrations during the flight of the aircraft, which caused the scattering point echo to be modulated in the azimuth direction, thereby

generating the ghost image. The azimuth phase error of the target was compensated using the PGA algorithm; however, the premise of this algorithm is azimuth-invariant; therefore, it cannot compensate the 2D defocus caused by the 3D wobble, as shown in Figure 9(b). Thus, the ship target was extracted from its locating area and transformed into the 1D range domain by azimuth IFFT; the 1D image migration correction was performed using envelope cross-correlation, and the image was processed using time-frequency analysis. It can be known from the time-frequency effect of STFT that although the defocus of the ship target could be removed,

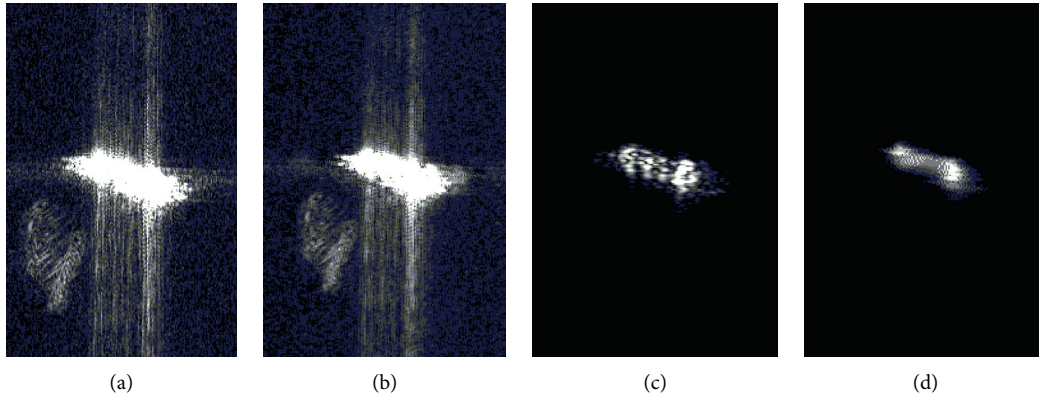


FIGURE 9: (a) RD ship; (b) minimum entropy-PGA ship; (c) STFT ship; and (d) SST-STFT ship.

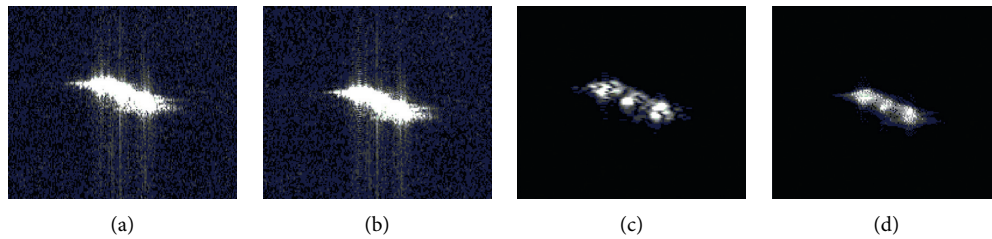


FIGURE 10: (a) RD ship; (b) minimum entropy-PGA ship; (c) STFT ship; and (d) SST-STFT ship.

TABLE 3: Comparison table of multialgorithm parameters for measured ship targets.

	WVD	Chirplet	STFT	CWT	SST-CWT	SST-STFT
Image SNR	-195.7247	-37.1570	1.9422	0.1548	8.9529	12.4246
Image entropy	0.6903	0.5549	0.2266	0.1161	0.0392	0.1960

there was still a certain degree of distortion in the image. This is because the time-frequency atoms used in the STFT algorithm have a fixed size and shape, which cannot fully fit the time-frequency spectrum of multicomponent signal, resulting in a stretched time-frequency spectrum, as shown in Figure 9(c). Meanwhile, the SST-STFT algorithm could obtain a more finely focused image of the ship target. The defocus of scattering points in both directions caused by ship wobble was removed. Furthermore, the ship's bow, stern, and the middle deck main structure could be clearly observed in the time-frequency spectrum, as shown in Figure 9(d). Figure 10 shows another defocusing ship in the measured data, and the imaging effect is also consistent with the above conclusion.

Table 3 shows the performance parameters of image signal-to-noise ratio (SNR) and image entropy for various algorithms of measured ships. By comparison, the SST-STFT algorithm proposed in this paper is better than other time-frequency analysis methods such as SST-CWT, CWT, and STFT. This is mainly because the synchronous compression algorithm correlates the ship target signal with the algorithm template and improves the time-frequency clustering, which is equivalent to filtering the sea clutter. If the image SNR is larger, it shows that the ability to remove

noise is stronger, and if the image entropy is smaller, the image focus is better.

#### 4. Conclusions

Based on the scenario of imaging stationary and moving ship targets on the vast sea surface, this paper proposed a block sparse compressed sensing method to solve the challenge of massive data processing and storage for phased array SAR. This algorithm used the echo signals received by each antenna array, and the JBOMP algorithm was adopted to obtain the 1D block sparse range image of each ship target. In addition, the range gate positions of multiple targets were determined, which played a positive role in accurately estimating the Doppler parameters of the targets. In the azimuth focusing process, each target was imaged separately, thereby avoiding the phase error compensation problem caused by the different translation and rotation characteristics of different targets. The SST-STFT time-frequency analysis algorithm was conducive to acquire accurate time-frequency imaging of the ships and particularly improved the reconstruction ability under low signal-to-noise (S/N) ratio conditions, thereby making it more favorable for the

accurate imaging of ships in high sea conditions. Simultaneously, as multiple antennas received echoes of the same area from multiple limited angles, the Doppler frequency diversity was increased, and the lateral resolution of the targets was improved. This algorithm not only greatly overcomes the shortcoming of massive data processing for multiantenna arrays, but also improves the performance for suppressing sea clutter, target positioning, and estimating the motion attitudes of targets.

### Data Availability

The data used to support the findings of this study are included within the article.

### Conflicts of Interest

The authors declare that they have no conflicts of interest.

### Acknowledgments

This work was supported by the National Natural Science Foundation of China for General Program under Grant no. 61971163.

### References

- [1] A. Torre, "Compact SAR: a flexible multimission SAR satellite," in *Proceedings of the 2015 IEEE 5th Asia-Pacific Conference on Synthetic Aperture Radar (APSAR)*, pp. 91–93, Singapore, September 2015.
- [2] J. H. G. Ender, P. Berens, A. R. Brenner et al., "Multi channel SAR/MTI system development at FGAN: from AER to PAMIR, Geoscience and remote sensing symposium," in *Proceedings of the 2002 IEEE International IGARSS'02*, pp. 1697–1701, Toronto, Canada, June 2002.
- [3] M. Cohen, A. Larkins, P. L. Semedo et al., "NovaSAR-S low cost spaceborne SAR payload design, development and deployment of a new benchmark in spaceborne radar," in *Proceedings of the 2017 IEEE Radar Conference (RadarConf17)*, Seattle, WA, USA, August 2017.
- [4] X. Bai, R. Tao, Z. Wang, and Y. Wang, "ISAR imaging of a ship target based on parameter estimation of multicomponent quadratic frequency-modulated signals," *IEEE Transactions on Geoscience and Remote Sensing*, vol. 52, no. 2, pp. 1418–1429, 2014.
- [5] M. Liu, P. F. Wang, Z. G. Wang et al., "Multidimensional motion parameters estimation for multi-SAR system using the cubic phase function," *IEEE Transactions on Geoscience and Remote Sensing*, vol. 56, no. 6, pp. 3210–3221, 2018.
- [6] L. Wang, D. Y. Zhu, and Z. D. Zhu, "Study on ship imaging using SAR real data," *Journal of Electronics & Information Technology*, vol. 29, no. 2, pp. 401–404, 2007.
- [7] Z. R. Pan, H. T. Fan, and Z. M. Zhang, "Nonuniformly-rotating ship refocusing in SAR imagery based on the bilinear extended fractional Fourier transform," *Sensors*, vol. 20, no. 550, pp. 1–14, 2020.
- [8] Y. C. Jiang and H. Y. Wang, "Hybrid SAR/ISAR imaging of ship targets based on parameter estimation," *Remote Sensing Letters*, vol. 8, no. 7, pp. 657–666, 2017.
- [9] M. Martorella, D. Pastina, F. Berizzi, and P. Lombardo, "Spaceborne radar imaging of maritime moving targets with the cosmo-SkyMed SAR system," *IEEE Journal of Selected Topics in Applied Earth Observations and Remote Sensing*, vol. 7, no. 7, pp. 2797–2810, 2014.
- [10] G. X. Wang, Z. M. Wang, and W. W. Wang, "SAR image super-resolution based on sparse cauchy distribution," *Journal of Astronautics*, vol. 29, no. 1, pp. 299–303, 2008.
- [11] N. Fu, L. R. Cao, and X. Y. Peng, "Compressed sensing of block-sparse signals recovery based on subspace," *Acta Electronica Sinica*, vol. 39, no. 10, pp. 2338–2342, 2011.
- [12] F. Weike, Y. Li, and S. Motoyuki, "Near range radar imaging based on block sparsity and cross-correlation Fusion algorithm," *IEEE Journal of Selected Topics in Applied Earth Observations and Remote Sensing*, vol. 11, no. 6, pp. 2079–2089, 2018.
- [13] M. J. Lü, W. F. Chen, and S. Q. Xia, "Random Chirp frequency-stepped signal ISAR imaging algorithm based on joint block-sparse model," *Journal of Electronics & Information Technology*, vol. 40, no. 11, pp. 2614–2620, 2018.
- [14] I. Daubechies, J. Lu, and H.-T. Wu, "Synchrosqueezed wavelet transforms: an empirical mode decomposition-like tool," *Applied and Computational Harmonic Analysis*, vol. 30, no. 2, pp. 243–261, 2011.
- [15] D. Li, H. Liu, X. Gui, and X. Zhang, "An efficient ISAR imaging method for maneuvering target based on synchrosqueezing transform," *IEEE Antennas and Wireless Propagation Letters*, vol. 15, pp. 1317–1320, 2016.